Screening of Cathode Materials for Inert-Substrate-Supported Solid Oxide Fuel Cells

F. Grimm[a], N.H. Menzler[a], P. Lupetin[b], O. Guillon[a,c]

[a] Forschungszentrum Jülich GmbH, Institute of Energy and Climate Research (IEK),
IEK-1: Materials Synthesis and Processing, Jülich, Germany
[b] Robert Bosch GmbH, Corporate Sector Research and Advance Engineering, Renningen, Germany;
[c]JARA-Energy, Jülich, Germany

Beside the standard manufacturing routes for ESCs and ASCs, the co-firing of an all-ceramic inert supported cell concept makes it possible to increase the marketability of SOFCs. In this way, the co-firing temperature of 1100°C<T<1300°C is a compromise between the electrolyte requiring high temperatures and low-temperature cathode sintering. This process has an impact on the microstructure of the cathode layer, on the number of triple-phase boundaries and the respective performance in terms of the polarization resistance of the cathode quantified by impedance measurements. In the present study, thirteen different cathode materials were examined by SEM, XRD and EIS. These cathode materials range from well-known perovskite materials, e.g. LSCF and LSC, to the new Ruddlesden-Popper phases, e.g. $La_4Ni_3O_{10}$, $La_3Ni_2O_7$, displaying a strong influence of the co-firing temperature e.g. cathode decomposition. These findings underline the need for precisely tailoring the cathodic properties to the manufacturing route and therefore lead to a reconsideration of cathodes which are commonly known to display low electrocatalytic activity as they might offer the required thermal stability.

Introduction

Solid oxide fuel cells (SOFCs) can be subdivided into four major cell types: electrode, electrolyte (ESC), metal (MSC) and inert-supported cells (ISC). Each cell type has its own advantages and disadvantages. (1) In general, the challenges that has to be overcome to allow a successful market entry of this technology is the reduction of production costs and the guarantee of the lifetime. Notably, the number of manufacturing steps required (e.g. shaping, casting, coating, cutting, handling), the sintering conditions and the cost of each layer play a crucial role in the cost of the different cell types. (2) The Comparison of these different cell designs with respect to the scale-up of the manufacturing process serves to underline the crucial factors: material prices and process costs. Hence, reducing the cell costs is a combination of reduction of material prices (e.g. using low-cost materials for the thick substrate layer), optimized cell architecture (use a thin electrolyte layer to keep the ohmic losses and the required operating temperature at a minimum) and process optimization (single co-firing heat-treatment vs. cost-intensive vacuum sintering steps). The inert-supported cell (ISC) potentially fulfills all of these criteria, whereby the cheap inert-support material can be applied at the fuel or air side. This concept has , for instance, been used by Rolls-Royce (3) and TOTO (4).

As part of a publicly funded R&D project (KerSOLife 100), an inert-supported cell (ISC) with forsterite doped with Zn and Ca as support material was investigated. Forsterite, an abundant and cheap magnesium silicate, was applied at the air side. The whole cell was manufactured in one single heat-treatment step at 1100°C<T<1300°C. To the best of our knowledge, the effects of the use of forsterite as support material combined with a low-cost co-firing manufacturing route on cell performance and lifetime have not yet been investigated in depth. Previous work has shown that cathode optimization is necessary to improve cell performance in the inert-substrate-supported concept. To date, the performance of the cell is limited by Zn–Mn spinel formation at the triple-phase boundaries. Moreover, co-firing at 1100°C<T<1300°C limits the possibility to adjust the final microstructure. (5, 6)

The aim of this study was to identify a cathode material capable of exhibiting high electrocatalytic activity in terms of low polarization resistances (R_{pol}) after co-firing at relatively high temperatures (for cathode sintering) 1100°C<T<1300°C. To this end, impedance measurements on co-fired (cathode and current collector) symmetrical cells were performed. Furthermore, the interactions of the considered cathode materials with the inert support were investigated to finally recommend a cathode for the targeted ISC.

Experimental

Thirteen different cathode materials were investigated with respect to their high-temperature stability, electrochemical performance and reaction tendency. To investigate the reaction tendency, inks of the different cathodes were screen-printed on a forsterite green plate, an inert magnesium silicate (Mg_2SiO_4) doped with Zn and Ca, with a wet layer thickness (WLT) of 272µm. The cathode ink consisted of 62.75 wt% cathode powder, 20.85 wt% terpineol (DuPont) and 16.4 wt% TM (transport medium containing 6 wt% 45 cp ethyl cellulose and terpineol).

To investigate the influence of co-firing at 1100°C<T<1300°C, electrochemical impedance spectroscopy was performed on electrolyte supported symmetrical cells, having a cathode and current collector on both sides. To reproduce the effect of forsterite during co-firing 20wt% forsterite was added to the current collector (CCL) of some cells. Yttria-stabilized zirconia (8YSZ, 200µm; Kerafol), screen-printed with a gadolinia-doped ceria (GDC) barrier layer (WLT=35 µm), was used as the substrate for the symmetrical cells. This was sintered at 1300°C for 5h.

Two series of samples were prepared. In the first series, named "pure", the cathode-ink and the CCL consisting of $La_{0.6}Sr_{0.4}MnO_3$ (LSM) were subsequently screen printed on the GDC-layer. The second sample series, named "mixed", has the same layout of the samples "pure", but 20wt% forsterite was added to the CCL. The screen printed layers have the following properties: WLT= 65µm and 2x173µm respectively. Both sample types were sintered at 1100°C<T<1300°C in air after screen printing of the cathode and CCL layers. The symmetrical cell layout are shown schematically in Figure 1

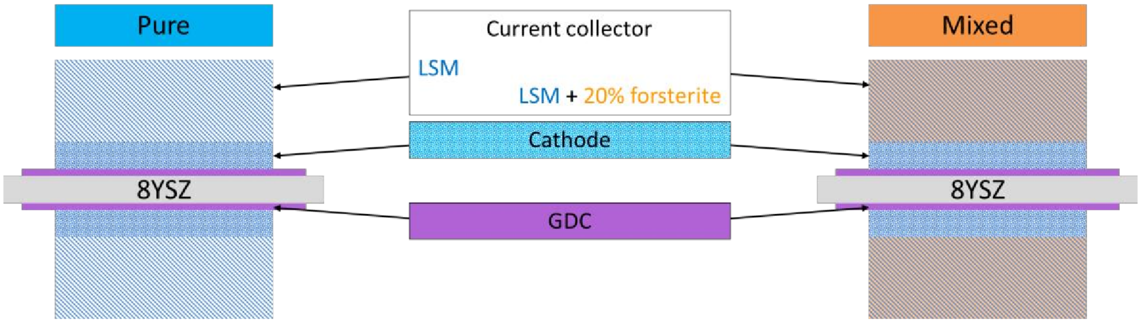

Figure 1. Symmetrical cell layout for "pure" (no forsterite) and "mixed" (with forsterite added to LSM CCL)

The materials investigated in this study were chosen among oxides with perovskite (ABO_3) or Ruddlesden-Popper phases ($A_{n+1}B_nO_{3n+1}$). The perovskite phases can be subdivided into (i) ferritic phases, such as: $La_{0.58}Sr_{0.4}Co_{0.2}Fe_{0.8}O_3$ (LSCF), $La_{0.58}Sr_{0.4}FeO_3$ (LSF), $Pr_{0.58}Sr_{0.4}Co_{0.2}Fe_{0.8}O_3$ (PSCF), $La_{0.58}Ca_{0.4}Co_{0.2}Fe_{0.8}O_3$ (LCCF), $(La_{0.9}Sr_{0.1})_{0.95}Fe_{0.7}Mn_{0.3}O_3$ (LSFM_95S1M3), $(La_{0.8}Sr_{0.2})_{0.95}Fe_{0.2}Mn_{0.8}O_3$ (LSFM_95S2M8), (ii) Titanate phases: $SrTiO_3$ (STO), $SrTi_{0.75}Fe_{0.25}O_3$ (STF25), $CaTi_{0.5}Fe_{0.5}O_3$ (CTF); and (iii) cobaltate phases: $La_{0.58}Sr_{0.4}CoO_3$ (LSC). The analyzed Ruddlesden-Popper phases are $La_3Ni_2O_7$ (La3Ni2) and $La_4Ni_3O_{10}$ (La4Ni3).

LSCF was chosen as it is currently the state-of-the-art cathode for anode-supported (ASC) SOFCs and has a high performance when thin-film electrolytes are used (7). LSF and LSC were selected to separately characterize the effect of the respective B-site perovskite elements, (Fe and Co, respectively). Furthermore, LSC is known to be more electrocatalytically active than LSCF. (8) The electrocatalytic activity of LSF is lower than the one of LSCF, although LSF exhibits better temperature stability. (9). With PSCF and LCCF, we wanted to investigate the effect of the replacement of Sr and La on the A-Site of the perovskite. Additionally, LCCF could exhibited more stable behavior compared to LSCF, as Ca has an atomic radius which only differs slightly from that of La (r_{Ca}=1.34 Å; r_{La}=1.36 Å and r_{Sr}=1.44 Å [36]). The atomic radii mismatch in relation to La is therefore minimized using Ca instead of Sr. (10) In order to exclude possible influences of different compositions, the overall stoichiometric composition of the perovskites $(A_{0.58}A'_{0.4})B_{0.2}B'_{0.8}O_3$ were kept constant. 2% A-site understoichiometry, was chosen as it represents the current state-of-the-art LSCF composition. (8) The LSFM compositions were chosen to demonstrate the influence of low and high Mn concentrations at the B-site in comparison to the currently used LSM/8YSZ. Titanates were chosen as STO is known to be stable and sulfur-tolerant. STF25 was used to display the influence of Fe at the B-side compared to STO, and CTF was used to exclude Sr as it is known to be reactive. Ruddlesden-Popper phases were chosen as they are classified as cathodes that perform well. (11, 12) Furthermore, with the two compositions, La4Ni3 and La3Ni2, the effect of an absence of Sr, Ca, Ti and Fe can be analyzed.

LSCF, LSC, LSF and PSCF were synthesized in-house via a spray pyrolysis route. Nitrates were used as precursors and were added to the combustion chamber for the reaction. The amount of the nitrates was chosen according to the desired stoichiometry of the nominal composition reported in table I. STO is commercially available (Sigma Aldrich). LSFM 95S1M3, LSFM 95S2M8, LCCF, La4Ni3 and La3Ni2 were synthesized using the Pechini method. STF25 was synthesized in previous work (13) and CTF was synthesized by liquid-phase synthesis.

The cation composition of each cathode powder (e.g. Table I) was analyzed by inductively coupled plasma optical emission spectrometry (ICP-OES) to verify the real final composition of the powder.

TABLE I. Nominal composition and composition determined via ICP-OES of the synthesized cathode materials**.**

Cathode	Nominal Composition	Calculated Composition according to ICP-OES
LSCF	$La_{0.58}Sr_{0.4}Co_{0.2}Fe_{0.8}O_3$	$La_{0.587\pm0.018}Sr_{0.405\pm0.012}Co_{0.202\pm0.006}Fe_{0.787\pm0.024}O_3$
PSCF	$Pr_{0.58}Sr_{0.4}Co_{0.2}Fe_{0.8}O_3$	$Pr_{0.581\pm0.017}Sr_{0.403\pm0.012}Co_{0.201\pm0.006}Fe_{0.798\pm0.024}O_3$
LSF	$La_{0.58}Sr_{0.4}FeO_3$	$La_{0.585\pm0.018}Sr_{0.403\pm0.012}Fe_{0.992\pm0.030}O_3$
LSC	$La_{0.58}Sr_{0.4}CoO_3$	$La_{0.595\pm0.018}Sr_{0.404\pm0.012}Co_{0.981\pm0.029}O_3$
LCCF	$La_{0.58}Ca_{0.4}Co_{0.2}Fe_{0.8}O_3$	$La_{0.581\pm0.017}Ca_{0.394\pm0.012}Co_{0.196\pm0.006}Fe_{0.810\pm0.024}O_3$
LSFM_95S1M3	$(La_{0.9}Sr_{0.1})_{0.95}Fe_{0.7}Mn_{0.3}O_3$	$(La_{0.892\pm0.028}Sr_{0.101\pm0.003})_{0.95}Fe_{0.701\pm0.021}Mn_{0.306\pm0.009}O_3$
LSFM_95S2M8	$(La_{0.8}Sr_{0.2})_{0.95}Fe_{0.2}Mn_{0.8}O_3$	$(La_{0.852\pm0.026}Sr_{0.193\pm0.006})_{0.95}Fe_{0.192\pm0.006}Mn_{0.765\pm0.023}O_3$
STO	$Sr_{0.5}Ti_{0.5}O_3$	$Sr_{0.493\pm 0.015}Ti_{0.507\pm0.015}O_3$
STF25	$SrTi_{0.75}Fe_{0.25}O_3$	$Sr_{1.048\pm0.031}Ti_{0.68\pm0.021}Fe_{0.263\pm0.008}O_3$
CTF	$Ca_{0.5}Ti_{0.45}Fe_{0.05}O_3$	$Ca_{0.506\pm0.015}Ti_{0.445\pm0.013}Fe_{0.050\pm0.001}O_3$
La4Ni3	La4Ni3O10	$La_{4.01\pm0.12}Ni_{2.99\pm0.09}O_{10}$
La3Ni2	La3Ni2O7	$La_{3\pm0.09}Ni_{2\pm0.06}O_7$

For phase analysis, and to validate the successful synthesis of the different cathode materials, a crystallographic analysis was carried on via X-ray diffraction using the Bragg–Brentano configuration (D4 Endeavor, Bruker AXS, Cu Kα1,2 radiation, λα=1.5418 Å).

Furthermore, the high-temperature stability of the investigated cathode materials was studied by comparing the XRD diffractogram of the respective raw and sintered cathode materials. To do so, samples were prepared by pressing 2g of the respective cathode powder into pellets with a diameter of 22mm applying 5kN for 2 minutes. We will refer to this sample as cathode_only. These pellets were then sintered at 1100°C<T<1300°C and subsequently analyzed by XRD measurements.

Electrochemical impedance spectroscopy (EIS) was used to measure the performance of each cathode material in terms of their respective polarization resistance (Rpol). The measurements were performed with an Alpha A High Performance Frequency Analyzer (Novocontrol Technologies) at a frequency range of 10^6 - 10^{-1} Hz and an a voltage of 20mV. The EIS_cathode samples were prepared by screen printing on 8YSZ substrates (200µm, Kerafol) a GDC barrier layer (WLT=35µm). The substrates were then sintered at T=1300°C for 5 h. Afterwards the respective cathode layer (D=12mm; WLT=65µm) and LSM current collector (pure or mixed with 20% forsterite) was screen printed on top (D=12mm; WLT=2x173µm) and then fired at 1100°C<T<1300°C.

Cross sections of the EIS_cathode and cathode_forsterite samples were subsequently obtained by embedding in epoxy, grinding, and then polishing with silica suspension. The specimens were sputtered with platinum to ensure sufficient electrical conductivity for investigations with a scanning electron microscope (SEM) (Zeiss Ultra55 with EDX from Oxford Instruments; INCAEnergy400 and Feico Phenom).

The properties of the different cathode inks are listed in Table II. The particle size was measured using a Horiba LA 950 V2 analyzer (Retsch Technology GmbH, Haan, Germany). Viscosity was measured with a rheometer (Anton Paar MCR 301) at a shear rate of 109 s-1.

TABLE II. Properties of the different cathode inks which were screen-printed on the Mg silicate support material. Viscosity was measured at a shear rate of 109 s^{-1}. All values are rounded to the second decimal place**.**

Cathode	**Synthesis method**	**Particle size**			**Viscosity at 109 s^{-1}**
		$d_{(10)}$	**$d_{(50)}$**	**$d_{(90)}$**	
LSCF	Spray pyrolysis	0.63	0.88	1.21	22.9
PSCF	Spray pyrolysis	0.60	0.82	1.10	13.4
LSC	Spray pyrolysis	0.61	0.85	1.16	12.7
LSF	Spray pyrolysis	0.58	0.77	1.00	13.8
LCCF	Pechini method	0.40	0.80	2.48	13.3
LSFM_95S1M3	Pechini method	0.61	0.88	1.26	11
LSFM_95S2M8	Pechini method	0.60	0.79	1.05	13.8
STO	Commercial	0.30	0.90	2.46	7.9
STF25	Pechini method	0.52	0.80	1.22	15.4
CTF	liquid-phase synthesis	0.59	0.82	1.13	13.1
La4Ni3	Pechini method	0.42	0.70	1.57	8.9
La3Ni2	Pechini method	0.60	0.80	1.04	7

In order to exclude any possible influences of different particle sizes, the difference of the $d_{(10)}$, $d_{(50)}$, and $d_{(90)}$ was kept as small as possible among the thirteen cathode inks (by ball milling the different cathode powders). The focus placed on the respective $d_{(50)}$ value. In summary, five different sample types were prepared and analyzed:

I) Cathode_forsterite:
screen-printed cathode inks on forsterite green plates and sintered

II) Cathode_only pellets:
cathode powder (2g) pressed into pellets and sintered

III) Cathode_mixed pellets:
cathode powder (1g) mixed with forsterite powder (1g) and sintered

IV) EIS_cathode_pure:
cathode ink and LSM CCL screen-printed on sintered 8YSZ+GDC

V) EIS_cathode_mixed:
cathode ink and LSM+20wt% forsterite CCL screen-printed on sintered 8YSZ+GDC

Results

Crystallographic characterization of the secondary phases

The low-cost manufacturing route involves the co-firing of the whole cell at 1100°C<T<1300°C. However, these relatively high firing temperatures may have a negative effect on the cathodes. To validate the stability of the different cathodes, cathode_only pellets were heat-treated and analyzed with respect to their phase stability via XRD. If a secondary phase is formed after heat treatment it is listed in Table III.

TABLE III. XRD measurements: comparison of the cathodes before and after heat treatment by heat-treating the cathode_only pellets at 1100°C<T<1300°C. For comparison LSCF, LSFM and STO are marked in grey.

Cathode	**Secondary phases after T<1300°C**
LSCF	$SrFeO_{2.8064}$
PSCF	Sr_2FeO_4
LSF	
LCCF	$LaCo_{0.5}Fe_{0.5}O_3$
LSFM_95S1M3	$LaFeO_3$
LSFM_95S2M8	
STO	
STF25	
CTF	
LSC	$LaCoO_{2.934}$
La4Ni3	$La_3Ni_2O_7$
La3Ni2	

For the crystallographic characterization of the secondary phases, XRD measurements were performed on cathode_mixed samples. The different secondary phases formed after co-firing at T<1300°C are listed in Table IV.

TABLE IV. Quantification of the secondary phases formed after heat treatment of the cathode_mixed pellets. For better comparison LSCF, LSFM and STO are shown in gray.

Cathode	**Secondary phases formed during co-firing**			
LSCF	$Sr_2Mg(Si_2O_7)$	$Sr_2La_8(SiO_4)_6O_2$	$Fe_{1.71}Mg_{1.43}O_4$	
PSCF	$Sr_2Mg(Si_2O_7)$	$Sr_2Pr_8(SiO_4)_6O_2$	$Fe_{1.71}Mg_{1.43}O_4$	
LSF	$Sr_2Mg(Si_2O_7)$	SiO_2	Ca_2SiO_4	$ZnFe_2O4$
LCCF	$Ca_3Mg(SiO_4)_2$	$CaLa_4(SiO_4)_3O$		
LSFM_95S1M3	Fe_3O_4	$La_{9.33}(Si_6O_{26})$		
LSFM_95S2M8	La_2O_3	$La_{0.7}Sr_{0.3}FeO_3$		
STO				
STF25	$Sr_2Mg(Si_2O_7)$	Fe_2MgO_4		
CTF	$CaMgSiO_4$	Fe_2MgO_4		
LSC	Sr_2Si	$SrSi_2$	$Co_{1.76}Zn_{13.24}$	
La4Ni3	$La_9Mg_{0.5}Si_6O_{26}$	$La_2NiO_{4.003}$		
La3Ni2	$La_9Mg_{0.5}Si_6O_{26}$			

LSCF_forsterite evolves three different phases, whereas LSFM_95S1M3_forsterite only evolves two, and for ST_forsterite no secondary phase at all were detected. These results are in good agreement with the SEM images in Figure 1 as LSCF_forsterite displays the strongest and ST_forsterite the lowest reaction tendency with forsterite. Note that the detection limit of the XRD device lies at ≈1wt%, explaining the absence of any secondary phase for STO, which is visible in Figure 1 (C), in Table III.

Interactions between magnesium silicate support substrate and various cathodes

The reaction tendency of thirteen different cathode materials was studied and analyzed with the aim of identifying a cathode displaying a stable trend after heat treatment at 1100°C<T<1300°C.

All cathodes reacted with forsterite; however, the reactions can be subdivided into three types: (A) formation of reaction layers and secondary phases at the interface and within the bulk of the reaction partners, (B) formation of island secondary phases throughout all layers and accumulation of them at the cathode-forsterite interface and (C) formation of secondary phases within the bulk of cathode and forsterite. These different reaction types are shown in Figure 2 with the examples of (A) LSCF-forsterite; (B) LSFM-95S1M3-forsterite and (C) STO-forsterite.

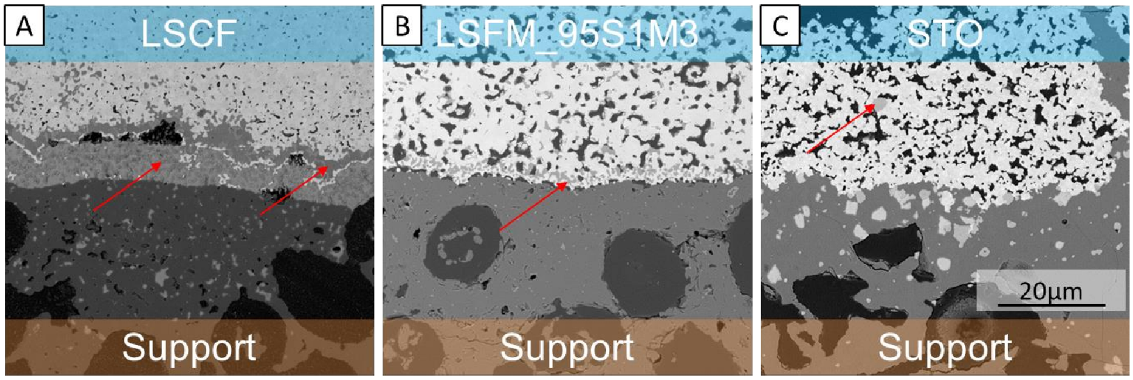

Figure 2. SEM images of the interaction samples (A) LSCF_forsterite, (B) LSFM_forsterite and (C) STO_forsterite. Red arrows mark the secondary phases which are formed after co-sintering.

LSCF_forsterite (Figure 1 (A)) evolves a thin (≈2µm) and a thick (≈7µm) reaction layer. In contrast, LSFM_forsterite (Figure 1 (B)) only displays secondary phases with a high concentration close to the interface of LSFM and forsterite and some within the bulk of the cathode. In STO_forsterite secondary phases are detected in the bulk of forsterite and STO. It is worth noting, that no secondary phases were detected via XRD on ST_mixed pellet as the amount of these phases are too small (cf. Table III).

The high-temperature stability of all the cathode materials listed in Table III is in good agreement with the findings from the SEM cross sections (Figure 2). LSCF_only and LSFM_95S1M3 display the formation of a secondary phase while STO_only is stable at 1100°C<T<1300°C.

Electrochemical characterization of the cathode materials

The performance of each cathode material was measured in terms of polarization resistance. The goal is the identification of a cathode suitable for the co-firing manufacturing route and, displaying, a good performance after sintering in contact with forsterite. Therefore, symmetrical cell architectures were used for each cathode material (cf. Figure 1). By comparing the "pure" and "mixed" cell layouts, it is possible to visualize the impact of the formation of secondary phases with forsterite. The ohmic resistance (R_{ohm}) and polarization resistance (R_{pol}) can be derived from the Nyquist plot obtained. The R_{ohm} comprises the ohmic resistance of the ion conductors (electrolytes and barrier layer), the intrinsic resistance of the measurement setup and the contacting of the sample. Since the focus of this work lies on the cathode only R_{pol} was considered.

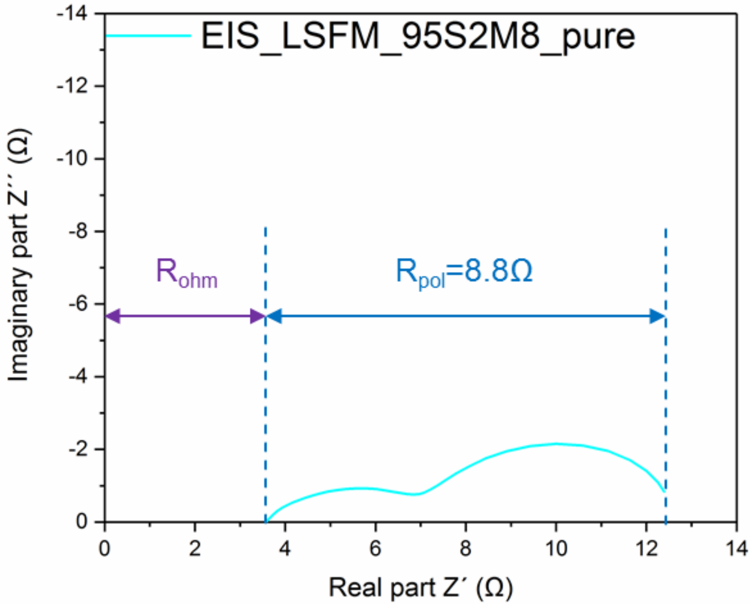

Figure 3. Nyquist plot for the sample LSFM_95S2M8_pure. In the plot the can be ohmic (R_{ohm}) and polarization (R_{pol}) parts are shown.

The R_{pol} value can then be related to the active surface area of the sample (D=12mm; A=1.1cm²) by using equation [1]. The values obtained for each cathode material (pure and mixed) are reported in Figure 4.

$$R_{pol}\ (\Omega) * A/2\ (cm^2) = R_{pol;area}\ (\Omega * cm^2) \qquad [1]$$

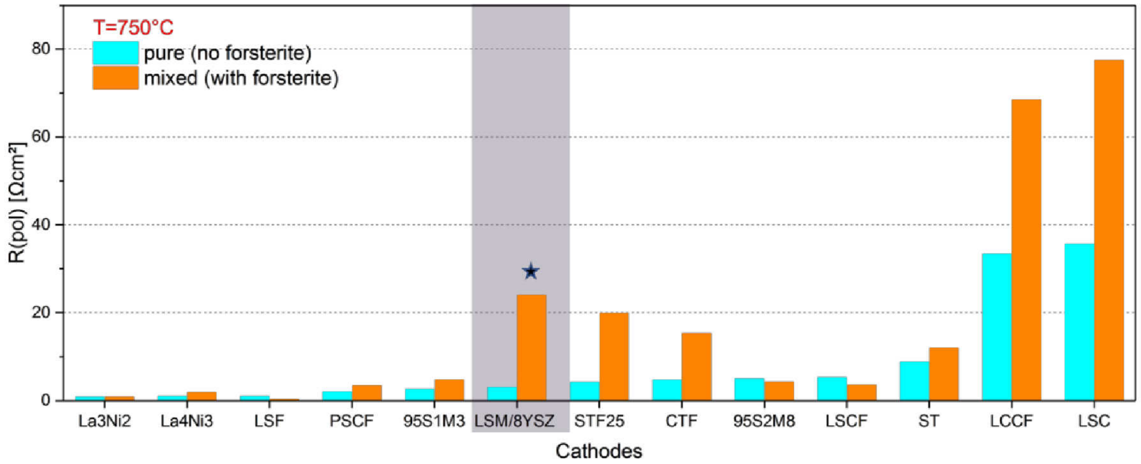

Figure 4. Bar chart with the respective R_{pol} values of each cathode material for the two setups "pure" and "mixed". The current state-of-the art cathode LSM/8YSZ within the ISC is marked in purple. The value for LSM/8YSZ_R_{pol}_mixed (★) is obtained with a different LSM composition.

Figure 4 shows that the lanthanum nickelates and LSF showed the best performance irrespective of whether the current collector is pure or mixed with forsterite. R_{pol} values for the samples "pure" and "mixed" with La3Ni2 (0.796930 and 0.814 Ωcm^2), La4Ni3: (0.94 and 1.79 Ωcm^2) and LSF (0.96 and 0.25 Ωcm^2) as cathode were obtained. LSC showed the highest R_{pol} with values of 35.61 (sample "pure") and 77.43 Ωcm^2 (sample "mixed") respectively.

GDC post-densification

The cross sections of the EIS_cathode samples were analyzed in order to obtain further insights into the differences of the measured R_{pol} values. A densification of the GDC was observed for some EIS_cathode samples. This was therefore systematically studied for all the cathodes listed in Table I.

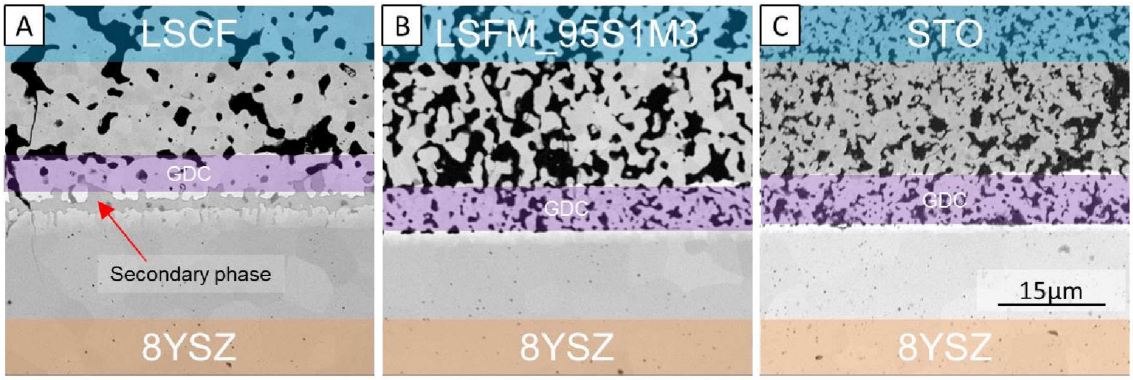

Figure 5. SEM cross sections (8YSZ-GDC-cathode) with the focus on the respective GDC (purple) layer for three different cathode materials: (A) LSCF, (B) LSFM_95S1M3 and (C) STO. For (A) LSCF an additional secondary phase appears (red arrow).

Figure 5 displays the cross sections of the EIS_cathode_pure samples for (A) LSCF, (B) LSFM_95S1M3 and (C) STO. For EIS_LSCF_pure, a post-densification of the GDC layer is visible as it is dense compared to the porous structure of the GDC layer for the samples EIS_LSFM_pure and EIS_STO_pure. All of the samples were analyzed, including those that were pure and those mixed with the different cathode materials. Dense GDC layers were only found for the EIS_cathode samples for LSCF, PSCF, LSC and LCCF. All other samples displayed a porous GDC layer similar to the one in Figure 5 (B) and (C). As this result suggests that Co is crucial for the GDC densification EDX-mapping on EIS_LSCF_pure was performed.

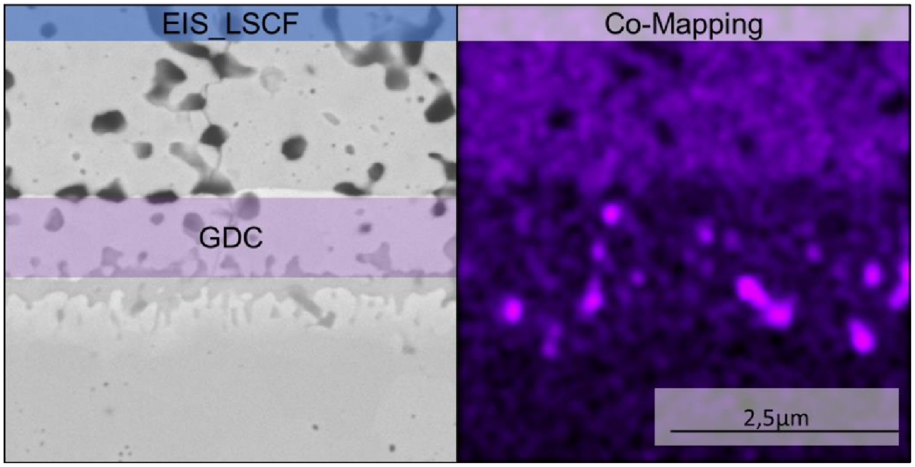

Figure 6. Cross sections of EIS_LSCF. On the left side the cross section is displayed, on the right side the related EDX Co-Mapping.

Figure 6 displays that Co strongly diffuses into the GDC and 8YSZ layer. Furthermore, the cathode materials display a difference in the porosity. A difference in porosity is obtained since the $d_{(50)}$ value (cf. Table II) was kept constant although the cathodes themselves have differences in their sintering ability.

Formation of secondary phases underneath the GDC layer

As already visible in Figure 4 (A), with EIS_LSCF_pure a secondary phase (marked with a red arrow) is formed underneath the GDC layer. This secondary phase was analyzed with EDX point scans. The results are shown in Figure 7.

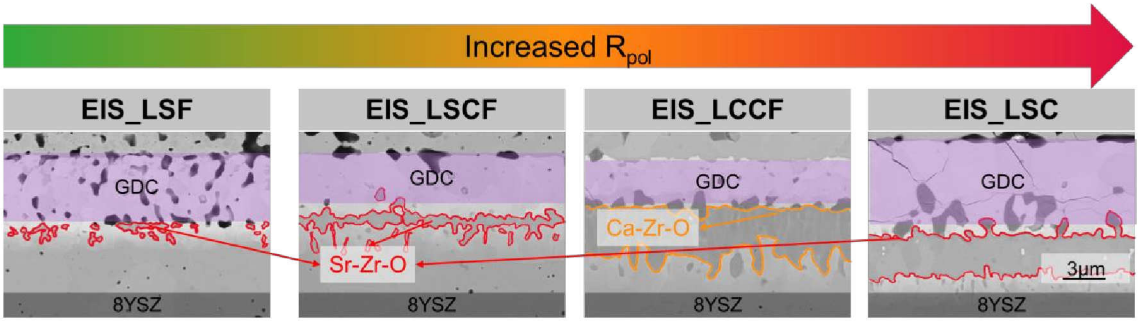

Figure 7. SEM cross sections of EIS_cathode_pure cells with LSF, LSCF, LCCF and LSC as the cathode material. The symmetrical cells are listed in ascending order of polarization resistance. The formation of the respective secondary phase underneath the GDC layer is highlighted in red and orange. EDX point scans were used to characterize the phases.

For LSF, LSCF, LCCF and LSC, the formation of a secondary phase containing Sr-Zr-O or Ca-Zr-O is observed underneath the GDC layer. It is assumed that these phases are $SrZrO_3$ and $Ca_{0.15}Zr_{0.85}O_{1.85}$. Furthermore, this secondary phase was also obtained for PSCF and STF25. However, the thickness and continuity of these layers vary with the respective cathode material analyzed. EIS_LSF only displays island-like secondary Sr-Zr-O phases. In contrast, EIS_LSC evolves a continuous and ≈3μm thick Sr-Zr-O layer. It was recently reported in literature that this highly insulating layer affects R_{pol}. (14, 15)

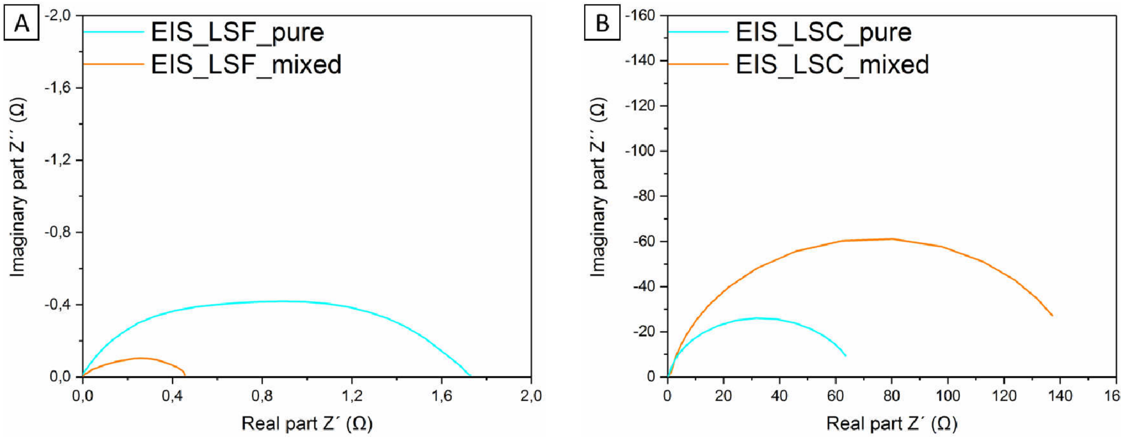

Figure 8. Nyquist plot of the samples (A) EIS_LSF and (B) EIS_LSC with a “pure” and “mixed” CCL.

The Nyquist-Plot of EIS_LSC (Figure 8 (B)) show a different response compared to EIS-LSF and this can be explained with the formation of the Sr-Zr-O insulating layer.

The EIS_cathode samples with LSFM_95S1M3, LSFM_95S2M8, STO, CTF, La3Ni2 and La4Ni3 did not display any secondary phase underneath the GDC layer.

Discussion

The results can be summarized in three different headings:

Interaction of various cathodes with magnesium silicate support substrate:

- High-temperature stability: Within the thirteen cathode materials (cf. Table III) investigated in this study, LSCF, PSCF, LCCF, LSFM_95S1M3, LSC and La4Ni3 are not stable in the considered co-firing temperature regime. For these materials, the formation of a secondary phase was observed after thermal treatment.
- Interactions of the cathodes with magnesium silicate support: All considered materials (cf. Table IV), except STO, react with forsterite. The number of evolved secondary phases detected by XRD is therefore in good agreement with the SEM images (cf. Figure 2). LSCF_forsterite displays a very strong interaction with forsterite as is visible in Table IV (detection of three different phases) and Figure 2 (A) since LSCF_forsterite forms optically dense reaction layers and numerous secondary phases. In contrast, Table IV does not show any reaction between STO and Forsterite (note the detection limit of the XRD device of ≈1wt %). This is in good agreement with the respective cross section (cf. Figure 2 (C)): compared to the other cathode_forsterite combination, STO_forsterite displays no reaction layer at the interface. Additionally, the XRD measurements show that the secondary phases mostly contain La-Si-O and Sr-Si-O phases and Mg-Si-O, thus indicating the high phase stability of the silicate.

Electrocatalytic activity of co-fired cathodes

- Electrochemical impedance spectroscopy: Figure 4 lists the measured R_{pol} values of the symmetrical cathode cells with a pure CCL and a CCL mixed with forsterite. Based on the EIS data of the symmetrical cells, La3Ni2, La4Ni3 and LSF are the best-performing cathodes with respect to the co-firing manufacturing process. These findings indicate that the catalytic activity is not associated with the formation of the number of secondary phases detected with XRD (cf. Table IV and IV) and SEM (cf. Figure 2). Based on the mentioned results, one would have expected EIS_LSF not to be among the best-performing cathodes. Additionally, the formation of secondary phases of LSF_forsterite improves the measured R_{pol} value from 0.96 (pure) to 0.25 Ωcm² (mixed). With an R_{pol} value of 35.61 Ωcm² (pure), LSC is the worst-performing cathode material. This is unusual, as LSC is in general known to be a good cathode with R_{pol} values of ≈ 0.01Ωcm² (T=750°C) (16) and LSF is classified as moderately good cathode material in the literature due to its R_{pol} values of ≈ 0.35 Ωcm² (T=700°C) (17). This result shows that a tailored development of all functional layers specific for the cell design plays a crucial role in obtaining high-performance cells. The huge difference can be explained by the slight decomposition of the cathode materials at high-sintering temperatures (cf. Table III) and the formation of a secondary phase underneath the GDC barrier layer.

- The secondary phase underneath the GDC barrier layer can be attributed to Sr-Zr-O for EIS_LSF and EIS_LSC (cf. Figure 7). In literature $SrZrO_3$ is known to be insulating. (18) As the processes associated with $SrZrO_3$ (blocking of oxygen-ion transport) occur within the frequency range of cathode polarization, this secondary phase will have an impact on the measured R_{pol} of the cathodes. Furthermore double-layer capacitances at the GDC/SrZrO3 interface, as it is explained in literature by Szász et al. (15), might be additional reasons. However, for LSF this is not the case as the Sr-Zr-O layer is not continuous and therefore conductive pathways, through which where the oxygen-ions can pass, are still available. (15)

<u>GDC Post-densification:</u>

- <u>GDC post densification</u> is observable for several samples e.g. LSCF. This effect is also described in literature and related to the presence of Sr, Fe and Co. (15) Due to the screening of thirteen different cathode materials the elements responsible for post-densification can be identified. For instance, in LCCF strontium was excluded, with LSF cobalt and with LSC iron. This enabled the systematic characterization of GDC post-densification resulting in the conclusion that only Co is responsible for GDC post-densification. This is supported by the EDX Co-Mapping shown in Figure 6.

Conclusion

High-temperature stability, good catalytic activity and a low reaction tendency of the cathode are important factors for the optimization of co-sintered SOFCs. Thirteen different cathode materials were tested in this study with the aim of identifying a high performance cathode material with low reaction tendency after co-firing at 1100°C<T<1300°C. In order to achieve this, the cathodes were analyzed with respect to their high-temperature stability and reactivity with the substrate material of the ISC. EIS measurements revealed that $La_3Ni_2O_7$, $La_4Ni_3O_{10}$ and $La_{0.58}Sr_{0.4}FeO_3$ are promising candidates as they are capable of being co-fired with the low-cost manufacturing route. The symmetrical cell with $La_{0.58}Sr_{0.4}FeO_3$ as cathode only displays the formation of small amounts of a Sr-Zr-O phase underneath the GDC layer. In contrast, LSC forms a continuous and thick Sr-Zr-O layer. This insulating layer has an impact on the R_{pol} which is used to classify the different cathode materials. Thus, cathodes which are generally known to exhibit moderate catalytic activity might be reconsidered (e.g. $La_{0.58}Sr_{0.4}FeO_3$ compared to $La_{0.58}Sr_{0.4}CoO_3$). It is important that the cathode is carefully chosen with respect to the manufacturing process (e.g. high heat treatment temperatures) of the cell.

Acknowledgments

The authors would like to thank Dr. Egbert Wessel, Institute of Energy and Climate Research – Microstructure and Properties of Materials (IEK-2), Forschungszentrum Jülich, for conducting EDX and WDX measurements. The authors would also like to thank Dr. Volker Nischwitz, Central Institute of Engineering, Electronics and Analytics – Analytics (ZEA-3), Forschungszentrum Jülich, for performing wet chemical analyses, and Dr. Falk Schulze-Küppers, Institute of Energy and Climate Research - Materials Synthesis and Processing (IEK-1), Forschungszentrum Jülich, for providing STF25. The project "KerSOLife100" (FKZ: 03ET6101) was funded by the German Federal Ministry for Economic Affairs and Energy (BMWi).

References

1. L. Blum, et al., *International Journal of Applied Ceramic Technology*, **2**, 482-492 (2005).
2. N.H.Menzler, et al., *Fuel Cells*, **14**, 96-106 (2014).
3. M. Cassidy, et al., *Fuel Cells*, **9**, 891-898 (2009).
4. S. Ando, et al., *Journal*, 23 (2014).
5. E. Matte, et al., *Journal of Power Sources*, **413**, 334-343 (2019).
6. E. Matte, et al., *Proceedings of European Fuel Cell Forum*, (2016).
7. F. Tietz, et al., *International Journal of Applied Ceramic Technology*, **4**, 436-445 (2007).
8. F. Han, et al., *Journal of Power Sources*, **218**, 157-162 (2012).
9. H. Yokokawa, et al., *Journal of Power Sources*, **182**, 400-412 (2008).
10. W. Lee, et al., *Journal of the American Chemical Society*, **135**, 7909-7925 (2013).
11. R.K. Sharma, et al., *Journal of Power Sources*, **325**, 337-345 (2016).
12. S.J. Skinner, J.A. Kilner, *Solid State Ionics*, **135**, 709-712 (2000).
13. F. Schulze-Kuppers, et al., *Separation and Purification Technology*, **147**, 414-421 (2015).
14. V. Wilde, et al., *ACS Applied Energy Materials*, **1**, 6790-6800 (2018).
15. J. Szász, et al., *Journal of The Electrochemical Society*, **165**, F898-F906 (2018).
16. P. Hjalmarsson, et al., *Solid State Ionics*, **179**, 1422-1426 (2008).
17. A. Nechache, et al., *Journal of Power Sources*, **258**, 164-181 (2014).
18. F.W. Poulsen, N. Vanderpuil, *Solid State Ionics*, **53**, 777-783 (1992).